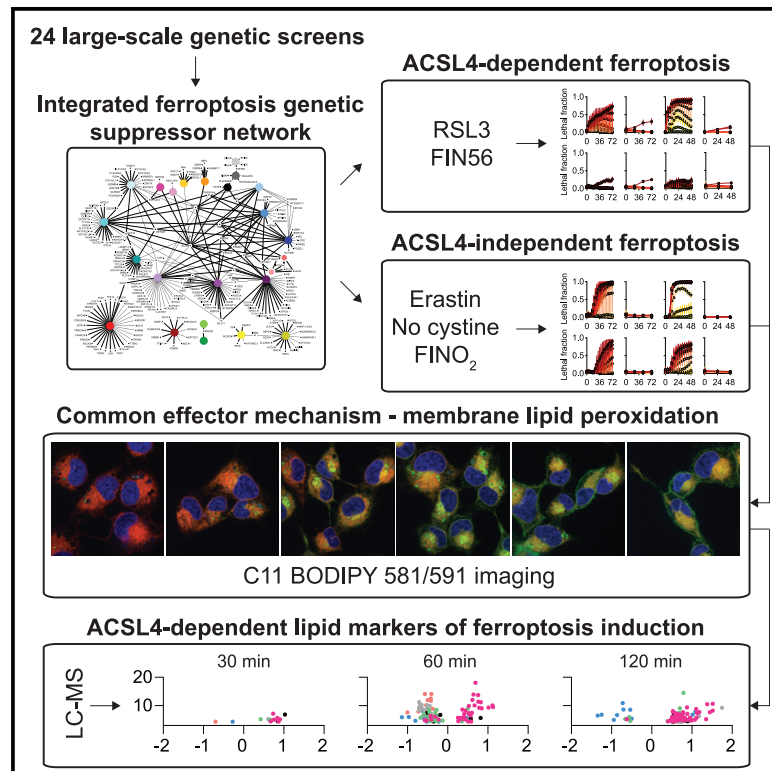


Cell Chemical Biology

Context-dependent regulation of ferroptosis sensitivity

Graphical abstract



Authors

Leslie Magtanong, Grace D. Mueller, Kevin J. Williams, ..., James A. Olzmann, Steven J. Bensinger, Scott J. Dixon

Correspondence

sjdixon@stanford.edu

In brief

The genetic regulation of ferroptosis remains poorly understood. Magtanong et al. demonstrate that *ACSL4*, *AGPS*, and other lipid metabolic genes are context-dependent ferroptosis regulators that are not universally essential for this process. Results suggest that there may not exist a single ferroptosis genetic regulatory mechanism in all cells and conditions.

Highlights

- An integrated genetic network reveals high variability in ferroptosis regulation
- *ACSL4* is most important for ferroptosis in response to direct GPX4 inhibition
- *AGPS* is not required for ferroptosis in all contexts
- Ferroptotic stimuli converge on plasma membrane lipid peroxidation

Brief Communication

Context-dependent regulation of ferroptosis sensitivity

Leslie Magtanong,¹ Grace D. Mueller,¹ Kevin J. Williams,^{2,3,4} Maximilian Billmann,⁵ Katherine Chan,⁶ David A. Armenta,¹ Jason Moffat,⁶ Charles Boone,⁶ Chad L. Myers,^{5,7} James A. Olzmann,^{8,9} Steven J. Bensinger,^{2,4} and Scott J. Dixon^{1,10,*}

¹Department of Biology, Stanford University, Stanford, CA 94305, USA

²Department of Microbiology, Immunology and Molecular Genetics, University of California, Los Angeles, Los Angeles, CA 90095, USA

³Department of Biological Chemistry, University of California, Los Angeles, Los Angeles, CA 90095, USA

⁴UCLA Lipidomics Laboratory, University of California, Los Angeles, Los Angeles, CA 90095, USA

⁵Department of Computer Science and Engineering, University of Minnesota-Twin Cities, 200 Union Street, Minneapolis, MN 55455, USA

⁶Department of Molecular Genetics, University of Toronto, Toronto, ON, Canada

⁷Program in Biomedical Informatics and Computational Biology, University of Minnesota-Twin Cities, 200 Union Street, Minneapolis, MN 55455, USA

⁸Departments of Molecular and Cell Biology and Nutritional Sciences and Toxicology, University of California, Berkeley, Berkeley, CA 94720, USA

⁹Chan Zuckerberg Biohub, San Francisco, CA 94158, USA

¹⁰Lead contact

*Correspondence: sjdixon@stanford.edu

<https://doi.org/10.1016/j.chembiol.2022.06.004>

SUMMARY

Ferroptosis is an important mediator of pathophysiological cell death and an emerging target for cancer therapy. Whether ferroptosis sensitivity is governed by a single regulatory mechanism is unclear. Here, based on the integration of 24 published chemical genetic screens combined with targeted follow-up experimentation, we find that the genetic regulation of ferroptosis sensitivity is highly variable and context-dependent. For example, the lipid metabolic gene acyl-coenzyme A (CoA) synthetase long chain family member 4 (*ACSL4*) appears far more essential for ferroptosis triggered by direct inhibition of the lipid hydroperoxidase glutathione peroxidase 4 (*GPX4*) than by cystine deprivation. Despite this, distinct pro-ferroptotic stimuli converge upon a common lethal effector mechanism: accumulation of lipid peroxides at the plasma membrane. These results indicate that distinct genetic mechanisms regulate ferroptosis sensitivity, with implications for the initiation and analysis of this process *in vivo*.

INTRODUCTION

Ferroptosis is a non-apoptotic cell-death process important in pathophysiology and as a potential target for new anti-cancer therapies (Jiang et al., 2021). This process can be induced by depleting cells of the thiol-containing amino acid cysteine, direct inhibition of the glutathione-dependent lipid hydroperoxidase glutathione peroxidase 4 (*GPX4*), and other means (Jiang et al., 2021; Shimada et al., 2016). These stimuli allow for iron-dependent accumulation of lipid peroxides to lethal levels (Conrad and Pratt, 2019; Wiernicki et al., 2020). Lipid peroxides form on specific polyunsaturated fatty acid (PUFA)-containing phospholipids, whose eventual destruction likely causes lethal permeabilization of the plasma membrane (Doll et al., 2017; Kagan et al., 2017; Magtanong et al., 2019). The regulation of ferroptosis sensitivity by intracellular signaling and metabolic networks remains poorly understood.

To search for conserved regulators of ferroptosis execution, we aggregated data from 24 large-scale chemical genetic screens. Unexpectedly, few genes appeared to be essential for ferroptosis execution in all contexts. Subsequent investigation

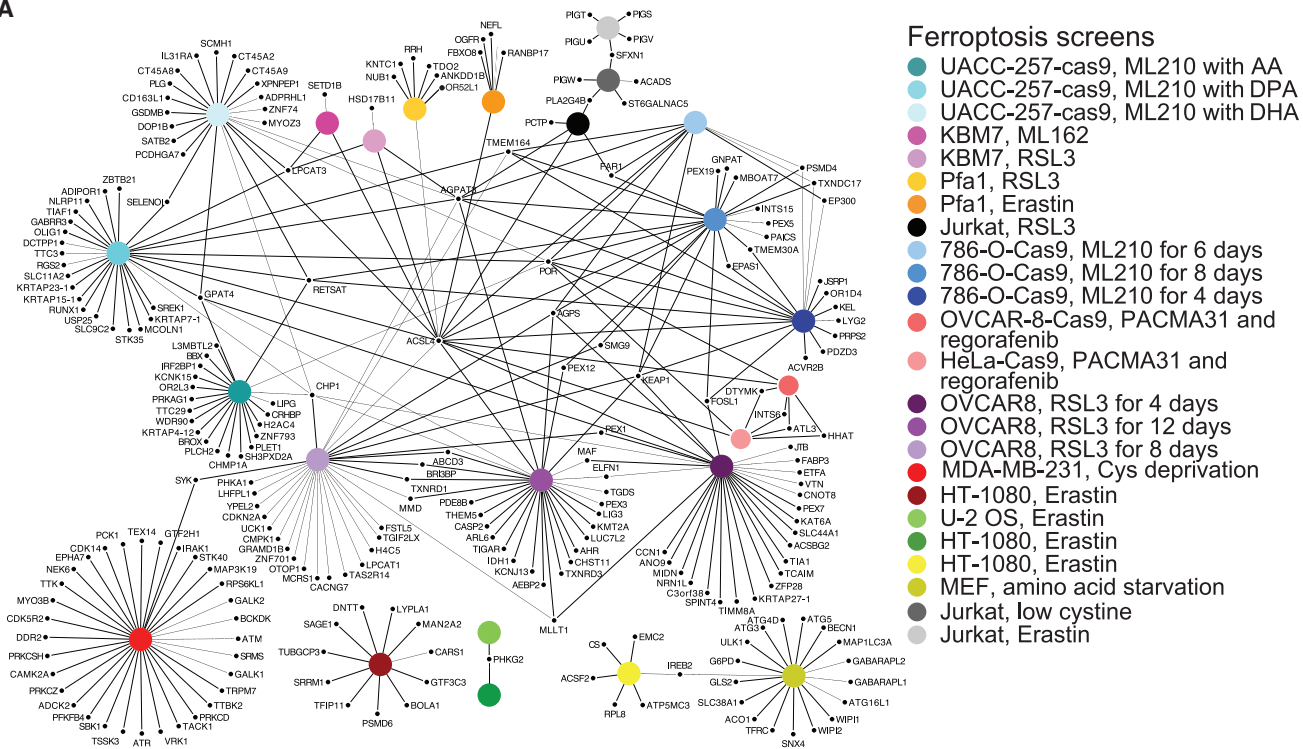
established that the key PUFA lipid metabolic enzyme acyl-coenzyme A (CoA) synthetase long chain family member 4 (*ACSL4*) is more important for the execution of ferroptosis following direct *GPX4* inactivation than cystine deprivation, while the key ether lipid synthesis enzyme alkyglycerone phosphate synthase (*AGPS*) is entirely dispensable for ferroptosis, at least in some contexts. This analysis reveals unanticipated diversity in the genetic regulation of ferroptosis sensitivity.

RESULTS

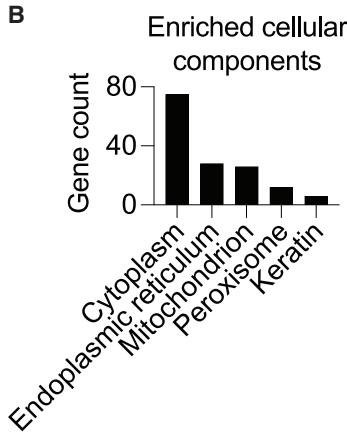
An integrated ferroptosis genetic suppressor network

To better understand the regulation of ferroptosis, we curated 24 published large-scale genetic loss-of-function screens for genes reported to promote ferroptosis execution in response to pro-ferroptotic stimuli (i.e., gene silencing or gene disruption inhibited cell death) (Table S1). These screens used 11 different cell lines and nine different pro-ferroptotic conditions, which we reasoned would provide a broad basis to search for common regulators of the ferroptosis mechanism. Across all 24 screens, a cumulative total of

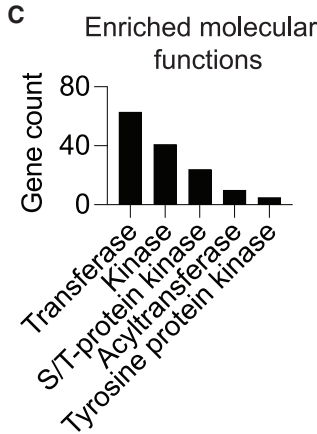
A



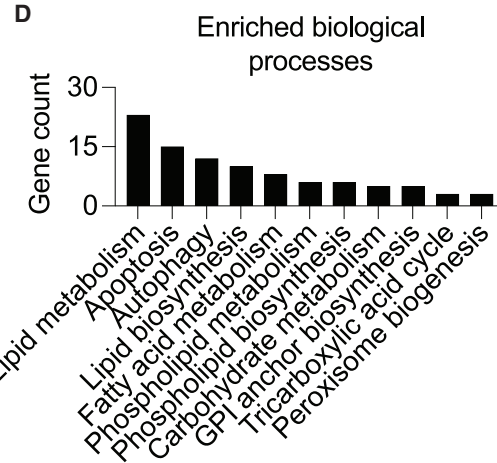
B



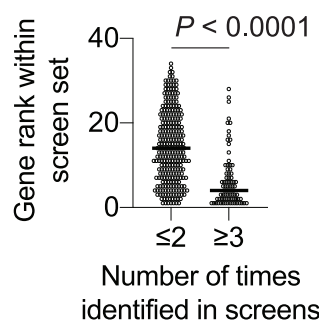
C



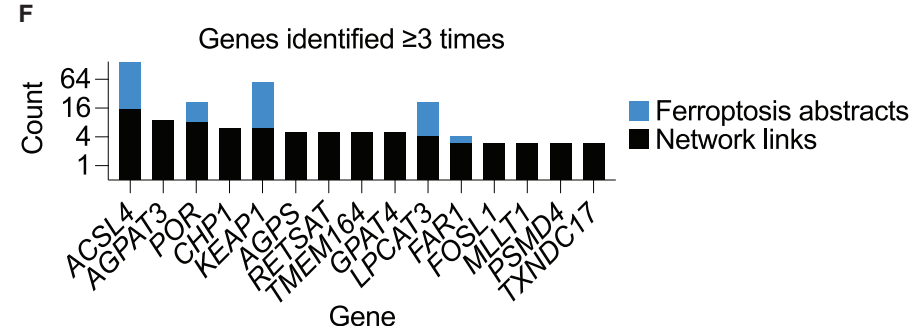
D



E



F



(legend on next page)

363 non-redundant genes were reported to suppress ferroptosis, with a median of 9.5 genes identified per screen (range = 1–34) (Table S2). To investigate further, we standardized gene annotations, mapped mouse genes to human orthologs where possible, filtered out pseudogenes and non-coding RNAs, and identified instances where the same gene was identified in more than one screen. This enabled us to construct an integrated network that ultimately linked the 24 screens to 239 unique protein-coding genes (Figure 1A). Annotating this network using the database for annotation, visualization, and integrated discovery (DAVID) bioinformatic resource (Huang et al., 2009) suggested significant enrichment for gene products localized to multiple intracellular compartments (cytoplasm, endoplasmic reticulum, peroxisome, and mitochondria) with diverse molecular functions (kinase activity, acyltransferase activity) and involved in a range of biological processes, most notably lipid metabolism (Figures 1B–1D). This analysis highlighted the potentially complex regulation of ferroptosis by spatially and functionally distinct cellular systems.

Based on the canonical model of ferroptosis regulation (Jiang et al., 2021), we initially hypothesized that our network would pinpoint many genes that were commonly essential for ferroptosis execution in all conditions. Of the 24 screens examined, 16 employed methods that should, in principle, have enabled the function of most genes in the genome to be assayed, while eight screens were conducted using reagent libraries targeted to different gene sub-sets (Table S1). This would make it impossible to identify any gene in all screens. However, to our surprise, only 24 genes were identified even two or more times, and 215 genes in the network (90% of the total) were identified in just one of 24 screens (Table S2). The lack of overlap between screens in the network could be explained by large numbers of false negatives in each individual screen; this possibility cannot easily be ruled out. However, an alternative possibility was that the regulation of ferroptosis sensitivity varied substantially between cell lines and lethal conditions.

To investigate further, we focused on 15 genes identified three or more times in our network. On average, these genes were more highly ranked in each screen than the 224 genes identified in less than three screens (Mann-Whitney U test, $p < 0.001$), consistent with higher confidence roles in ferroptosis regulation (Figure 1E). Indeed, among these genes, *ACSL4*, *LPCAT3*, *POR*, and *KEAP1* are validated ferroptosis regulators (Dixon et al., 2015; Doll et al., 2017; Forcina et al., 2022; Sun et al., 2016; Yan et al., 2021; Zou et al., 2020b), while *GPAT4*, *CHP1*, *RETSAT*, and *TXNDC17* are plausible ferroptosis regulators based on the functions of these genes in lipid metabolism and redox homeostasis (Espinosa and Arner, 2019; Pang et al., 2017; Zhu et al., 2019) (Figure 1F). Still, these 15 genes were identified,

on average, in only 20% of all screens (median = 5/24, range 3–15) (Figure 1F). Using data available through the Dependency Map portal (depmap.org), we considered and rejected the possibility that differences in basal gene expression or gene essentiality between cell lines provided a general explanation for the lack of overlap between screens (Figures S1A and S1B). For example, 786-O, OVCAR8, and HT-1080 cell lines expressed similar levels of *ACSL4* and *AGPS*, yet these lipid metabolic genes were identified as being essential for ferroptosis only in genome-wide screens conducted in 786-O and OVCAR8 cells. These findings suggested that the genetic regulation of ferroptosis could vary substantially between contexts.

ACSL4 is a context-specific ferroptosis regulator

As a case study to investigate the potential context-specific regulation of ferroptosis, we first focused on *ACSL4*. *ACSL4* is generally considered a universal ferroptosis regulator (Jiang et al., 2021), but there is also evidence that ferroptosis can be executed in the absence of this gene in some contexts (Chu et al., 2019; Shui et al., 2021). Overall, *ACSL4* was found more often than any other gene in our network (Figure 1C). Strikingly, however, *ACSL4* disruption was identified in 14/16 screens that induced ferroptosis by inhibiting GPX4 but only 1/8 of screens that induced ferroptosis by depriving cells of cystine (Figure 1A). While technical issues could explain some of these differences, we also considered the alternative possibility that *ACSL4* was more important for ferroptosis induced by direct GPX4 inhibition than cystine deprivation.

To investigate, we first conducted a new genome-wide CRISPR-Cas9 screen in human HAP1 haploid cells treated with the potent system x_c^- inhibitor erastin2. Overall, 340 genes were identified as significant modulators (enhancers or suppressors) of erastin2-induced cell death (false discovery rate [FDR] $q < 0.05$) (Figure 2A; Table S3). Disruption of genes that promote glutathione and cysteine synthesis (*GCLM*, *SLC7A11*, *CTH*, *CBS*), amino acid homeostasis (*ATF4*), and mechanistic target of rapamycin (mTOR) signaling (*TSC1*, *TSC2*, *NPRL2*, *DEPDC5*) all sensitized to erastin2, while disruption of *SFXN1* and *KEAP1* suppressed cell death, consistent with published findings (Conlon et al., 2021; Dixon et al., 2012, 2014; Dodson et al., 2019; Soula et al., 2020). By contrast, disruption of *ACSL4* and other lipid metabolic genes found in our network (e.g., *LPCAT3*, *AGPAT3*, *CHP1*) did not suppress erastin2-induced death in HAP1 cells (Figure 2B). Previously, we identified *ACSL4* and *LPCAT3* as essential for cell death in response to direct GPX4 inhibition in KBM7 cells (Dixon et al., 2015), from which HAP1 cells are derived, suggesting that these genes could, in theory, have been identified in our erastin2 screen if they were important regulators.

Figure 1. A literature-curated regulatory genetic network of ferroptosis suppressors

(A) A consensus ferroptosis regulatory network integrating results from 24 loss-of-function genetic suppressor screens. Each genetic screen is indicated by a large, uniquely colored circular node that corresponds to the cell line and ferroptosis-inducing condition employed. Each gene is represented by a small black node. Edges connect individual screens to specific genes.

(B–D) Network gene characterization using the database for annotation, visualization, and integrated discovery (DAVID) bioinformatic resource.

(E) Aggregate reported gene ranks for genes identified in ≤ 2 or ≥ 3 conditions in the consensus network in (A). Values closer to zero indicate the gene was a stronger hit.

(F) Number of times a given gene was identified in the network in (A), overlaid with number of abstracts reported in PubMed that mention the gene name and ferroptosis together.

See also Figure S1 and Tables S1 and S2.

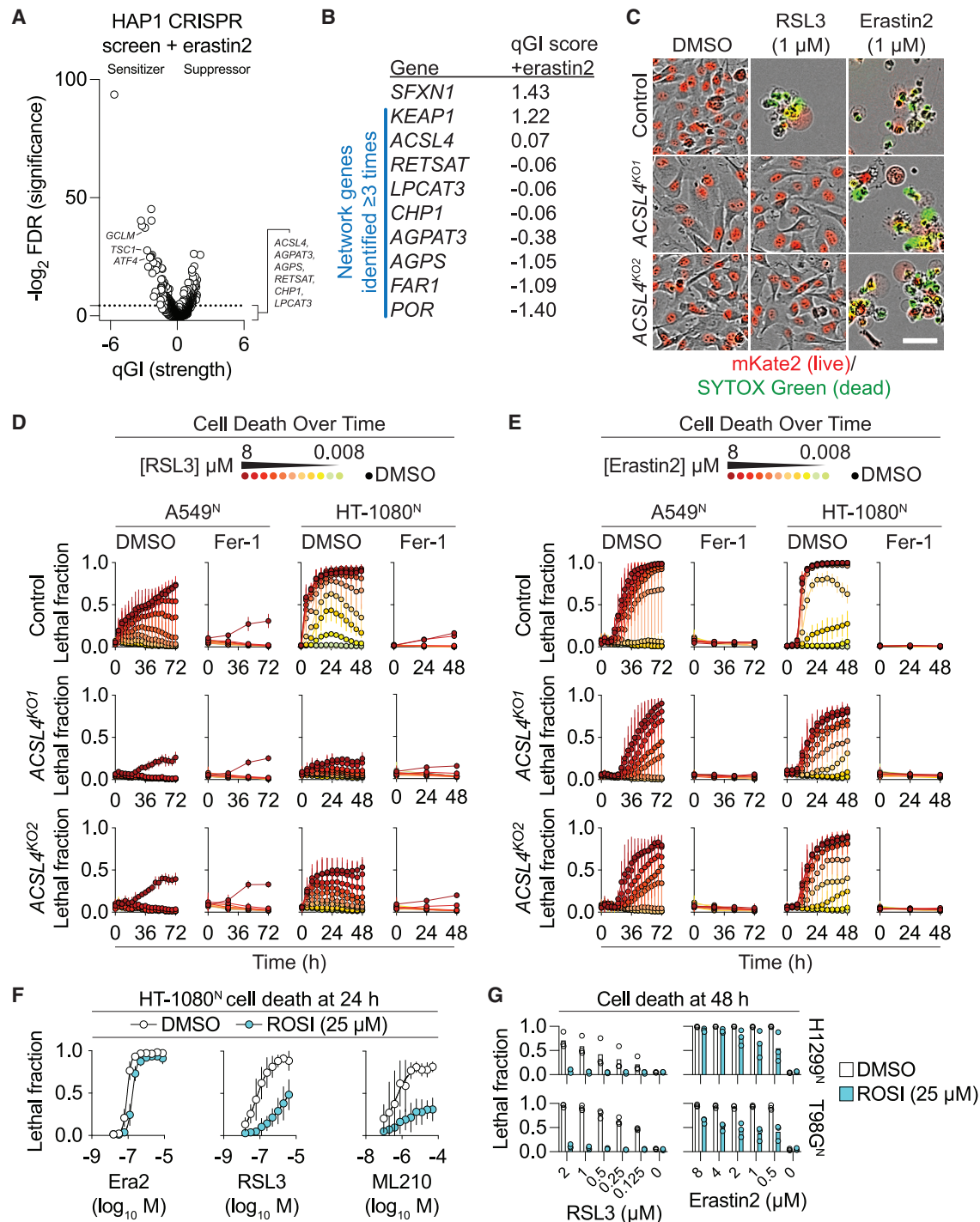


Figure 2. ACSL4 is required for ferroptosis in response to GPX4 inhibitors

(A) Results of a HAP1 CRISPR screen. Individual genes ($n = 17,800$) are plotted as circles. Select sensitizer genes are indicated. qGI, quantitative genetic interaction. Horizontal dotted line: FDR $q < 0.05$.

(B) Select gene qGI scores from (A).

(C) HT-1080^N cells imaged after 48 h treatment. Scale bar: 50 μm . Representative of three experiments.

(D and E) Lethal fraction dose-response curves over time for (D) RSL3- or (E) erastin2-treated cells \pm ferrostatin-1 (Fer-1, 1 μM). For lethal fraction, 0 = all cells alive, 1 = all cells dead.

(F and G) Lethal fraction of cells pre-treated for 24 h \pm rosiglitazone (ROSI) prior to lethal compound treatment.

Data in (D)–(F) are mean \pm SD from three independent experiments. Each data point in (G) is from one independent experiment.

See also Figures S2 and S3 and Table S3.

Next, we examined unmodified (Control) and clonal *ACSL4* gene-disrupted (i.e., knockout [KO]) HT-1080^N fibrosarcoma and A549^N non-small cell lung carcinoma (NSCLC) cell lines (Magtanong et al., 2019) (Figure S2A). Using a shotgun liquid chromatography coupled to mass spectrometry (LC-MS) lipidomics method (Hsieh et al., 2021), we confirmed that *ACSL4* disruption reduced the abundance of multiple PUFA-containing triacylglycerols and phospholipid species in both cell lines, especially those containing C22:6 acyl chains (Kagan et al., 2017) (Figures S2B and S2C). These cell lines express nuclear-localized mKate2 protein, which allowed us to precisely quantify cell death over time using the scalable time-lapse analysis of cell death kinetics (STACK) technique (Forcina et al., 2017). In line with our genetic network analysis, *ACSL4* disruption suppressed ferroptosis induced by the GPX4 inhibitor RSL3 more potently than ferroptosis induced by the system x_c^- inhibitor erastin2 or direct cystine deprivation (Figures 2C–2E and S2D). In all experiments, cell death was potently suppressed by the radical trapping antioxidant ferrostatin-1 (Fer-1), demonstrating that our lethal reagents were inducing cell death via ferroptosis (Figures 2D and 2E). RSL3 sensitivity was restored in HT-1080 *ACSL4*^{KO1} cells by re-expressing the long isoform of *ACSL4* (Kuch et al., 2014), confirming that effects on ferroptosis were due to *ACSL4* loss specifically (Figures S2E and S2F).

Given the unexpected nature of these results, we sought additional evidence that *ACSL4* was more important for ferroptosis induced by direct GPX4 inhibition than by cystine deprivation. Using isogenic HEK 293^N human embryonic kidney cells that do or do not express *ACSL4* (Magtanong et al., 2019), we again found that disruption of *ACSL4* more strongly reduced sensitivity to RSL3 than erastin2 (Figure S2G). Furthermore, in HT-1080^N and two additional cancer cell lines (H1299^N NSCLC and T98G^N glioblastoma), pre-treatment for 24 h with the small molecule *ACSL4* inhibitor rosiglitazone (Doll et al., 2017; Kim et al., 2001) also rendered cells more resistant to ferroptosis induced by RSL3 or the structurally distinct GPX4 inhibitor ML210 than to erastin2 (Figures 2F and 2G). Thus, *ACSL4* appeared more important for ferroptosis in response to direct GPX4 inhibition than cystine deprivation.

We recently reported that mTOR activity promotes ferroptosis in response to cystine deprivation but not GPX4 inhibition (Conlon et al., 2021). *ACSL4* may modulate mTOR activity through a lipid-dependent signaling mechanism (Orlando et al., 2015). Thus, we examined whether *ACSL4* disruption enhanced mTOR pathway activity, masking a protective effect for *ACSL4* deletion in response to cystine deprivation. Arguing against this possibility, *ACSL4* disruption in HT-1080 cells did not increase the phosphorylation of key mTOR substrates, and addition of the ATP competitive mTOR inhibitor INK128 to *ACSL4*^{KO1} cells did not allow for full inhibition of ferroptosis in response to erastin2, as would be expected if increased mTOR activity was masking the protective effect of *ACSL4* disruption (Figures S3A and S3B). Thus, altered mTOR signaling did not appear to explain why *ACSL4* was less important for ferroptosis execution in response to cystine deprivation than direct GPX4 inhibition.

We next considered the role of *ACSL4* in response to additional ferroptosis-inducing conditions. Cell death induced by the oxime-containing compound FIN56, which triggers GPX4 protein degradation (Shimada et al., 2016), was potently suppressed by *ACSL4* disruption, consistent with the requirement

for *ACSL4* function in ferroptosis triggered by GPX4 perturbation (Figure S3C). By contrast, ferroptosis induced by the endoperoxide-containing 1,2-dioxolane FINO₂, which directly promotes iron oxidation (Abrams et al., 2016; Gaschler et al., 2018), was only weakly inhibited by disruption of *ACSL4*, more like cells deprived of cystine (Figure S3D). *ACSL4* disruption did not alter sensitivity to compounds that trigger non-ferroptotic cell death, confirming that *ACSL4* is not a general regulator of cell death (Figure S3E). Collectively, these results suggested that *ACSL4* is a lethal context-specific regulator of ferroptosis sensitivity.

Ether lipid synthesis is not essential for ferroptosis

Analysis of our genetic network suggested that other lipid metabolism genes may, like *ACSL4*, play context-specific roles in ferroptosis regulation. In particular, we focused on *AGPS*, which encodes alkylglycerone phosphate synthase. *AGPS* is required for the synthesis of ether lipids, a special class of phospholipids proposed to be essential for ferroptosis execution (Zou et al., 2020a). However, *AGPS* was identified as a ferroptosis suppressor gene in only 5/24 screens cataloged in our network (Figure 1A) and was not detected in our HAP1 CRISPR screen with erastin2 (Figure 2A; Table S2). We therefore hypothesized that, like *ACSL4*, *AGPS* may play a context-specific role in ferroptosis regulation. To test this hypothesis, we generated *AGPS* gene-disrupted HT-1080^N cell lines (Figure 3A), where the abundance of numerous PUFA-containing ether lipids was substantially reduced (Figures 3A and 3B). Surprisingly, *AGPS* disruption had little effect on sensitivity to erastin2 or RSL3 (Figures 3C and S4A). These results were consistent with the structure of our genetic suppressor network and our HAP1 CRISPR screen, which suggested that *AGPS*-dependent ether lipid synthesis may play a context-specific, rather than universal, role in ferroptosis execution. These results also demonstrated that *AGPS*-dependent ether lipid synthesis may sometimes be entirely dispensable for ferroptosis, even in response to direct GPX4 inhibition, which distinguishes *AGPS* from *ACSL4*.

Notably, disruption of *AGPS* re-routed PUFA species from ether lipids into diacyl phospholipids such as PE 16:0/22:6 and PE 16:0/22:4 (Figure 3B). We hypothesized that the overall abundance of PUFAs in membrane phospholipids could be a more important determinant of ferroptosis sensitivity than the specific phospholipid class (i.e., diacyl versus ether lipid). Consistent with this possibility, pre-treatment with rosiglitazone suppressed ferroptosis to a similar extent in response to RSL3 in both HT-1080^N Control and *AGPS*^{KO1/2} cell lines (Figure 3D). We intended to perform the converse experiment in our *ACSL4* gene-disrupted cell lines using a published small molecule inhibitor of *AGPS*, ZINC-69435460 (termed here *AGPSi* [Piano et al., 2015]). However, exploratory experiments revealed that *AGPSi* alone sensitized our *AGPS* gene-disrupted cell lines to ferroptosis (Figures S4A and S4B). This suggests that *AGPSi* has a confounding off-target effect in connection with ferroptosis regulation and should be used with caution.

Distinct ferroptotic stimuli converge on a common effector mechanism

Ferroptosis is defined by the accumulation of lipid reactive oxygen species (ROS) within the cell and at the plasma membrane (Kagan et al., 2017; Magtanong et al., 2019; Torii et al., 2016).

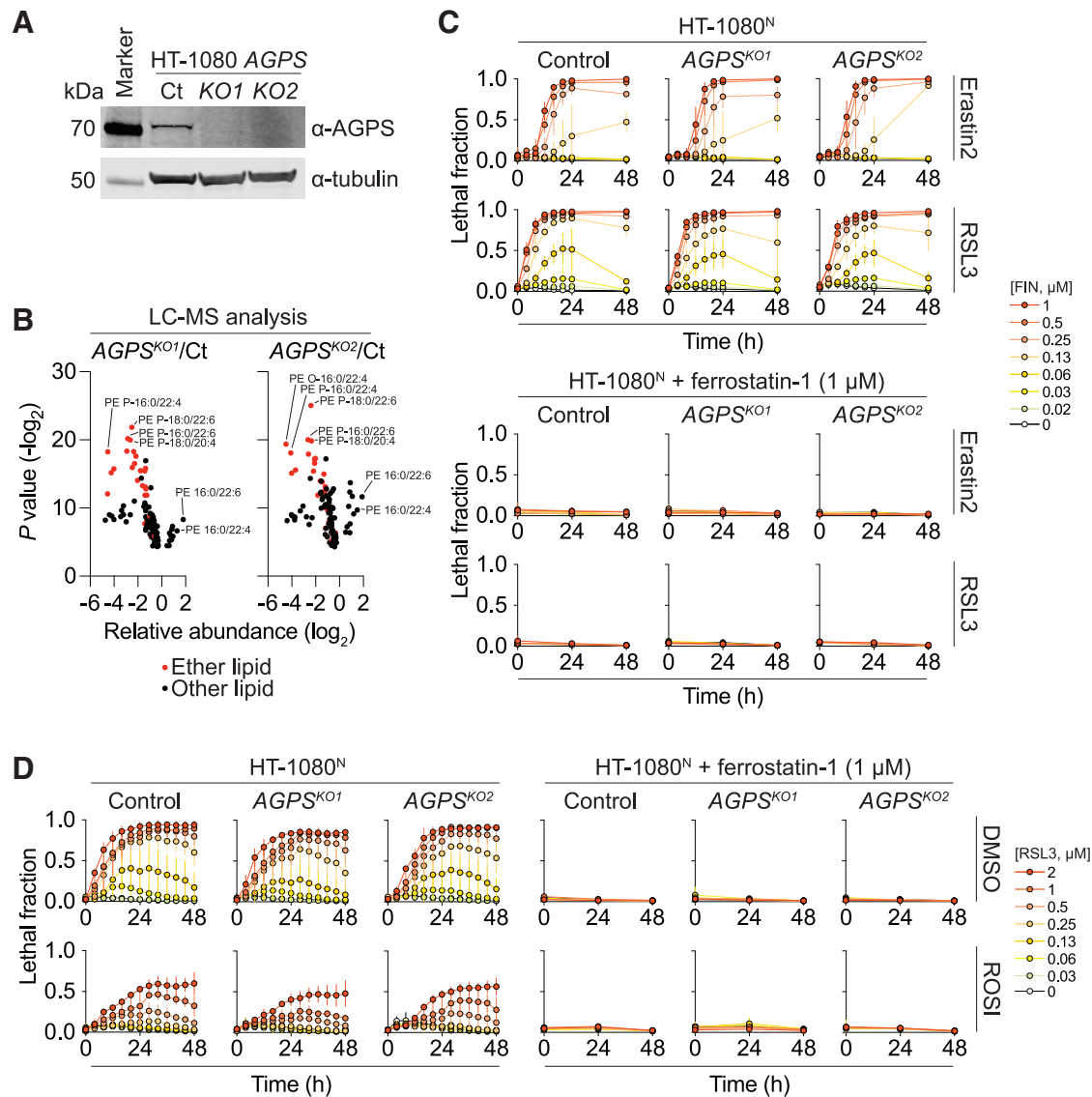


Figure 3. Ether lipids are dispensable for ferroptosis induction

(A) Protein expression in Control (Ct) and gene-disrupted (KO) cell lines.

(B) Relative lipid abundance in HT-1080^N control versus *AGPS*^{KO1/2} cells for significantly altered lipids ($p < 0.05$, Student's *t* test). PE, phosphatidylethanolamine; O, ether linked; P, vinyl ether linked.

(C) Lethal fraction dose-response curves over time. FIN, ferroptosis inducer.

(D) Lethal fraction dose-response curves over time of cells pre-treated for 24 h ± rosiglitazone (ROSI, 25 μM) prior to lethal compound treatment.

Data in (B) are mean of four independent experiments. Data in (C) and (D) are mean ± SD from three independent experiments.

See also [Figure S4](#).

Regardless of the means of induction, ferroptosis and ferroptosis-associated lipid peroxidation can be suppressed by common inhibitors, such as the radical trapping antioxidant Fer-1, suggesting that the terminal fate of ferroptotic cells must share certain commonalities (Dixon et al., 2012). To investigate whether specific lipid metabolic enzymes could influence spatial patterns of lipid ROS accumulation, we performed experiments in both HT-1080 Control and *ACSL4*^{KO1} cells. Lipid ROS accumulation was visualized using C11 BODIPY 581/591 (C11), a ratiometric probe (Magtanong et al., 2019; Pap et al., 1999). In response to erastin2, both HT-1080 Control and *ACSL4*^{KO1} cells

exhibited increased C11 oxidation prior to the onset of cell death, both in perinuclear regions and at the plasma membrane (Figure 4A). These results were consistent with the viability data and suggested that *ACSL4* status does not influence ferroptosis in response to cystine deprivation.

We next examined C11 oxidation in response to direct GPX4 inhibition. In control cells, RSL3 caused increased C11 oxidation within the cell and at the plasma membrane, much like treatment with erastin2 (Figure 4B). However, in *ACSL4*^{KO1} cells, C11 was oxidized at internal sites but not at the plasma membrane (Figure 4B). Even prolonged incubation with RSL3 of up to 8 h did

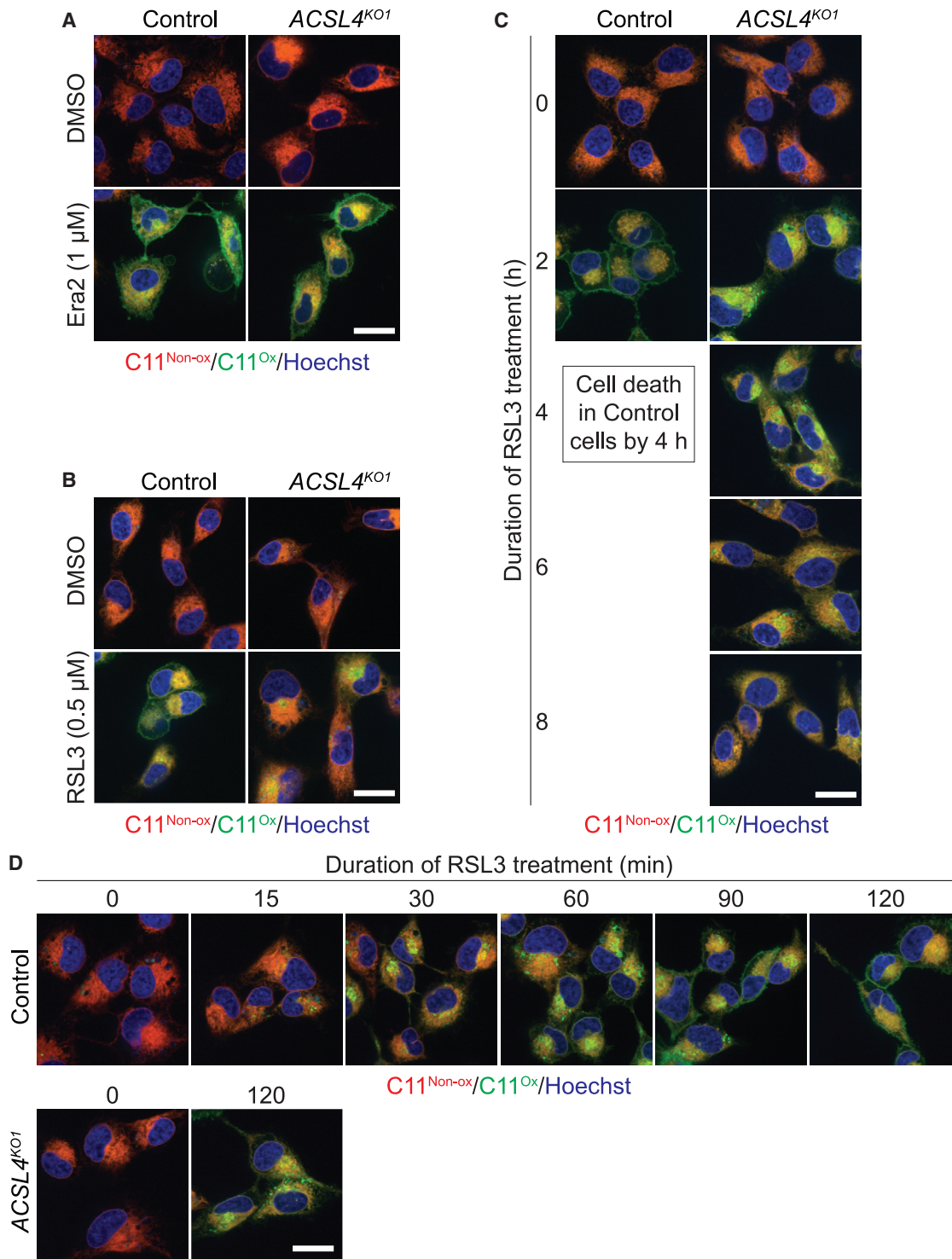


Figure 4. Context-dependent role for ACSL4 in lipid peroxidation spreading during ferroptosis

(A) HT-1080 control and ACSL4^{KO1} cells ± erastin2 (1 μM) for 10 h (Control) or 13 h (ACSL4^{KO1}). C11, C11 BODIPY 581/591; Non-ox, non-oxidized; Ox, oxidized. Scale bar: 20 μm.

(B–D) HT-1080 Control and ACSL4^{KO1} cells ± RSL3 (0.5 μM) for 2 h (B) or the indicated time points (C and D) prior to labeling with C11 and Hoechst.

For (A)–(D), two or more independent experiments were performed, and representative images from one experiment are shown.

See also [Figure S4](#).

not result in plasma membrane C11 oxidation in *ACSL4^{KO1}* cells, and these cells continued to proliferate over 72 h, suggesting that these cells remained functionally intact (Figures 4C and S4C). As noted, C11 oxidation in RSL3-treated *ACSL4^{KO1}* cells was observed at intracellular sites at 4 h, then faded such that by 8 h, little C11 oxidation was apparent (Figure 4C). Intracellular C11 oxidation was not as prominent inside Control cells after 2 h GPX4 inhibitor treatment (Figure 4C). In fact, in RSL3-treated Control cells, we observed bright internal C11 oxidation within 15 min and subsequent oxidation of plasma membrane C11 by 90 min (Figure 4D). Thus, C11 oxidation first occurs at the cell interior then at the plasma membrane in a manner that requires ACSL4 in response to GPX4 inhibition but not cystine deprivation.

Finally, we used shotgun LC-MS to correlate the observed changes in lipid oxidation with global alterations in lipid abundance in HT-1080 Control and *ACSL4^{KO1}* cells treated with RSL3 for 30, 60, or 120 min. The abundance of dozens of lipids was dynamically altered by RSL3 treatment, the vast majority in an ACSL4-dependent manner including numerous PUFA-containing TAGs that were increased by 30 min and diverse PEs that were decreased at 60 min, around the time lipid oxidation was first observed to reach the plasma membrane (Figure S4D). These complex changes define a lipidomic signature that correlates with the induction of ACSL4-dependent ferroptosis over time in response to direct GPX4 inhibition and the sequential accumulation of oxidized lipids at internal sites followed by the plasma membrane.

DISCUSSION

We find little overlap between genes identified as ferroptosis regulators in two dozen published genetic screens. New genome-wide CRISPR screening, as well as targeted gene editing, lipidomic analysis, and lipid ROS imaging, suggest context-specific roles for several genes in ferroptosis execution, most notably *ACSL4* and *AGPS*. Our results are consistent with previous evidence for context-specific ferroptosis regulatory mechanisms (Soula et al., 2020; Zille et al., 2022). Compared with other cell-death mechanisms like apoptosis or necroptosis, which appear to rely on a universal set of key effectors (Green, 2019), ferroptosis may be difficult to describe as a single, unitary lethal mechanism.

Our results suggest the existence of at least two distinct modes of ferroptosis execution defined by the requirement for ACSL4. ACSL4 is more important for the induction of ferroptosis in response to direct GPX4 inhibition than cystine deprivation or treatment with the iron oxidizing agent FINO_2 . ACSL4 is also dispensable for ferroptosis in response to p53 induction and photodynamic therapy (Chu et al., 2019; Shui et al., 2021). Thus, ACSL4-independent ferroptosis may be induced by diverse stimuli. How lethal lipid peroxidation occurs under these diverse conditions in the absence of ACSL4 remains to be clarified. One possibility is that distinct ACSL-family enzymes contribute to the pool of lipids that are oxidized in response to cystine deprivation.

The dynamics of lipid peroxidation during ferroptosis remains largely unclear. The long isoform of ACSL4, which restores sensitivity to GPX4 inhibitors in ACSL4 mutant cell lines

(Figures S2E and S2F), is predominantly localized to the endoplasmic reticulum (ER) (Kuch et al., 2014). ACSL4 may be necessary for the synthesis of PUFA-containing triacylglycerols or phospholipids in the ER that are required for, or are themselves the target of, lethal peroxidation, at least in response to direct GPX4 inhibition. It is unclear whether lipid peroxidation spreads from internal puncta and perinuclear membranes to the plasma membrane or whether internal sites are simply oxidized before lipids found at the plasma membrane. Regardless, it is remarkable that both direct GPX4 inhibition and cystine deprivation appear to converge on the peroxidation of plasma membrane lipids as a final common effector for the execution of ferroptosis.

Limitations of the study

We integrated genetic screening data obtained using diverse cell lines and lethal conditions. Technical differences between the design and execution of these screens could result in false negatives that contribute to the lack of concordant results. It is also difficult in loss-of-function screens to assess the role of essential genes in ferroptosis suppression, which could be better conserved than for non-essential genes. The lethal conditions and cell-based models examined here represent only a fraction of potential conditions where ferroptosis may be observed *in vitro* and *in vivo*. Our results were also obtained using cancer cell lines, and the role of ACSL4 in lipid oxidation in non-cancer cells and tissues could be different. It will be important to survey ferroptosis in more conditions to arrive at a clearer understanding of how plastic this mechanism may be in different contexts.

SIGNIFICANCE

Ferroptosis is a non-apoptotic cell death process whose genetic regulation appears to be complex. We find little overlap in the genes identified as essential for ferroptosis in two dozen published genetic screens. Detailed investigation indicates that *ACSL4* is more important for the execution of ferroptosis in response to direct GPX4 inhibition than cystine deprivation. An implication of these findings is that it may be misleading to use *ACSL4* dependence as a universal test for the occurrence of this lethal process. Our results also do not support a general requirement for *AGPS* or other lipids in ferroptosis regulation, although they may be important in some contexts. Broadly, our results indicate that it may be impossible to define a single, unitary ferroptosis regulatory pathway. These findings highlight an inherent plasticity in the genetic regulation of ferroptosis.

STAR★METHODS

Detailed methods are provided in the online version of this paper and include the following:

- KEY RESOURCES TABLE
- RESOURCE AVAILABILITY
 - Lead contact
 - Materials availability
 - Data and code availability
- EXPERIMENTAL MODEL AND SUBJECT DETAILS
 - Cell lines and culture conditions

- **METHOD DETAILS**
 - Network construction and analysis
 - Shotgun lipidomics sample treatment, preparation and analysis
 - CRISPR/Cas9 genetic screen
 - Cell death analysis using STACK
 - Cell death assays
 - ACSL4 rescue experiments
 - CRISPR/Cas9 genome editing and DNA sequencing
 - Western blot analysis
 - C11 BODIPY 581/591 imaging
- **QUANTIFICATION AND STATISTICAL ANALYSIS**
- **ADDITIONAL RESOURCES**
 - Chemicals and reagents

SUPPLEMENTAL INFORMATION

Supplemental information can be found online at <https://doi.org/10.1016/j.chembiol.2022.06.004>.

ACKNOWLEDGMENTS

We thank T. Stearns, K. Aulakh, R. Clime, A. Habsid, A. Tong, and M. Costanzo for help with experiments and K. Woerpel, R. Skouta, and H. Xiao for reagents. M.B. and C.L.M. were partially supported by the National Science Foundation (1818293). J.M. and C.B. were supported by a Genome Canada DIG Phase 2 award. J.M. is a Canada Research Chair Tier 2 in Functional Genomics of Cancer, and C.B. holds a Canada Research Chair Tier 1 in Functional Genomics and Proteomics, is a fellow of the Canadian Institute for Advanced Research (CIFAR), and was supported by the Canadian Institutes of Health Research (PJT-180285). This work was also supported by awards from the National Institutes of Health to C.L.M. (R01HG005084 and R01HG005853), J.A.O. (R01GM112948), S.J.B. (HL146358), and S.J.D. (R01GM122923).

AUTHOR CONTRIBUTIONS

Conceptualization, L.M. and S.J.D.; methodology, L.M., G.D.M., K.J.W., and J.A.O.; investigation, L.M., G.D.M., K.J.W., M.B., K.C., and D.A.A.; writing – original draft, L.M. and S.J.D.; writing – review & editing, L.M., G.D.M., K.J.W., J.A.O., S.J.B., and S.J.D.; supervision, J.M., C.B., C.M., J.A.O., S.J.B., and S.J.D.

DECLARATION OF INTERESTS

J.A.O. is a member of the scientific advisory board of Vicinitas Therapeutics. S.J.D. is a co-founder of Prothegen and a member of the scientific advisory boards for Ferro Therapeutics and Hillstream BioPharma. J.A.O. and S.J.D. hold patents related to ferroptosis.

Received: July 30, 2021

Revised: April 11, 2022

Accepted: June 15, 2022

Published: July 8, 2022

REFERENCES

Abrams, R.P., Carroll, W.L., and Woerpel, K.A. (2016). Five-membered ring peroxide selectively initiates ferroptosis in cancer cells. *ACS Chem. Biol.* *11*, 1305–1312. <https://doi.org/10.1021/acschembio.5b00900>.

Aregger, M., Lawson, K.A., Billmann, M., Costanzo, M., Tong, A.H.Y., Chan, K., Rahman, M., Brown, K.R., Ross, C., Usaj, M., et al. (2020). Systematic mapping of genetic interactions for de novo fatty acid synthesis identifies C12orf49 as a regulator of lipid metabolism. *Nat. Metab.* *2*, 499–513. <https://doi.org/10.1038/s42255-020-0211-z>.

Brinkman, E.K., Chen, T., Amendola, M., and van Steensel, B. (2014). Easy quantitative assessment of genome editing by sequence trace decomposition. *Nucleic Acids Res.* *42*, e168. <https://doi.org/10.1093/nar/gku936>.

Christianson, J.C., Olzmann, J.A., Shaler, T.A., Sowa, M.E., Bennett, E.J., Richter, C.M., Tyler, R.E., Greenblatt, E.J., Wade Harper, J., and Kopito, R.R. (2011). Defining human ERAD networks through an integrative mapping strategy. *Nat. Cell Biol.* *14*, 93–105. <https://doi.org/10.1038/ncb2383>.

Chu, B., Kon, N., Chen, D., Li, T., Liu, T., Jiang, L., Song, S., Tavana, O., and Gu, W. (2019). ALOX12 is required for p53-mediated tumour suppression through a distinct ferroptosis pathway. *Nat. Cell Biol.* *21*, 579–591. <https://doi.org/10.1038/s41556-019-0305-6>.

Conlon, M., Poltorack, C.D., Forcina, G.C., Armenta, D.A., Mallais, M., Perez, M.A., Wells, A., Kahanu, A., Magtanong, L., Watts, J.L., et al. (2021). A compendium of kinetic modulatory profiles identifies ferroptosis regulators. *Nat. Chem. Biol.* *17*, 665–674. <https://doi.org/10.1038/s41589-021-00751-4>.

Conrad, M., and Pratt, D.A. (2019). The chemical basis of ferroptosis. *Nat. Chem. Biol.* *15*, 1137–1147. <https://doi.org/10.1038/s41589-019-0408-1>.

Dixon, S.J., Lemberg, K.M., Lamprecht, M.R., Skouta, R., Zaitsev, E.M., Gleason, C.E., Patel, D.N., Bauer, A.J., Cantley, A.M., Yang, W.S., et al. (2012). Ferroptosis: an iron-dependent form of nonapoptotic cell death. *Cell* *149*, 1060–1072. <https://doi.org/10.1016/j.cell.2012.03.042>.

Dixon, S.J., Patel, D.N., Welsch, M., Skouta, R., Lee, E.D., Hayano, M., Thomas, A.G., Gleason, C.E., Tatonetti, N.P., Slusher, B.S., and Stockwell, B.R. (2014). Pharmacological inhibition of cystine-glutamate exchange induces endoplasmic reticulum stress and ferroptosis. *Elife* *3*, e02523. <https://doi.org/10.7554/elife.02523>.

Dixon, S.J., Winter, G.E., Musavi, L.S., Lee, E.D., Snijder, B., Rebsamen, M., Superti-Furga, G., and Stockwell, B.R. (2015). Human haploid cell genetics reveals roles for lipid metabolism genes in nonapoptotic cell death. *ACS Chem. Biol.* *10*, 1604–1609. <https://doi.org/10.1021/acschembio.5b00245>.

Dodson, M., Castro-Portuguez, R., and Zhang, D.D. (2019). NRF2 plays a critical role in mitigating lipid peroxidation and ferroptosis. *Redox Biol.* *23*, 101107. <https://doi.org/10.1016/j.redox.2019.101107>.

Doll, S., Proneth, B., Tyurina, Y.Y., Panzilius, E., Kobayashi, S., Ingold, I., Irmeler, M., Beckers, J., Aichler, M., Walch, A., et al. (2017). ACSL4 dictates ferroptosis sensitivity by shaping cellular lipid composition. *Nat. Chem. Biol.* *13*, 91–98. <https://doi.org/10.1038/nchembio.2239>.

Espinosa, B., and Arnér, E.S.J. (2019). Thioredoxin-related protein of 14 kDa as a modulator of redox signalling pathways. *Br. J. Pharmacol.* *176*, 544–553. <https://doi.org/10.1111/bph.14479>.

Forcina, G.C., Conlon, M., Wells, A., Cao, J.Y., and Dixon, S.J. (2017). Systematic quantification of population cell death kinetics in mammalian cells. *Cell Syst.* *4*, 600–610.e6. <https://doi.org/10.1016/j.cels.2017.05.002>.

Forcina, G.C., Pope, L., Murray, M., Dong, W., Abu-Remaileh, M., Bertozzi, C.R., and Dixon, S.J. (2022). Ferroptosis regulation by the NGLY1/NFE2L1 pathway. *Proc. Natl. Acad. Sci. USA* *119*, e2118646119. <https://doi.org/10.1073/pnas.2118646119>.

Gaschler, M.M., Andia, A.A., Liu, H., Csuka, J.M., Hurlocker, B., Vaiana, C.A., Heindel, D.W., Zuckerman, D.S., Bos, P.H., Reznik, E., et al. (2018). FINO2 initiates ferroptosis through GPX4 inactivation and iron oxidation. *Nat. Chem. Biol.* *14*, 507–515. <https://doi.org/10.1038/s41589-018-0031-6>.

Green, D.R. (2019). The coming decade of cell death Research: five riddles. *Cell* *177*, 1094–1107. <https://doi.org/10.1016/j.cell.2019.04.024>.

Hsieh, W.Y., Williams, K.J., Su, B., and Bensinger, S.J. (2021). Profiling of mouse macrophage lipidome using direct infusion shotgun mass spectrometry. *STAR Protoc.* *2*, 100235. <https://doi.org/10.1016/j.xpro.2020.100235>.

Huang, D.W., Sherman, B.T., and Lempicki, R.A. (2009). Systematic and integrative analysis of large gene lists using DAVID bioinformatics resources. *Nat. Protoc.* *4*, 44–57. <https://doi.org/10.1038/nprot.2008.211>.

Inde, Z., Forcina, G.C., Denton, K., and Dixon, S.J. (2020). Kinetic heterogeneity of cancer cell fractional killing. *Cell Rep.* *32*, 107845. <https://doi.org/10.1016/j.celrep.2020.107845>.

- Jiang, X., Stockwell, B.R., and Conrad, M. (2021). Ferroptosis: mechanisms, biology and role in disease. *Nat. Rev. Mol. Cell Biol.* 22, 266–282. <https://doi.org/10.1038/s41580-020-00324-8>.
- Kagan, V.E., Mao, G., Qu, F., Angeli, J.P.F., Doll, S., Croix, C.S., Dar, H.H., Liu, B., Tyurin, V.A., Ritov, V.B., et al. (2017). Oxidized arachidonic and adrenic PEs navigate cells to ferroptosis. *Nat. Chem. Biol.* 13, 81–90. <https://doi.org/10.1038/nchembio.2238>.
- Kim, J.H., Lewin, T.M., and Coleman, R.A. (2001). Expression and characterization of recombinant rat acyl-CoA synthetases 1, 4, and 5. *J. Biol. Chem.* 276, 24667–24673. <https://doi.org/10.1074/jbc.m010793200>.
- Küch, E.M., Vellaramkalayil, R., Zhang, I., Lehnen, D., Brügger, B., Stremmel, W., Ehehalt, R., Poppelreuther, M., and Füllekrug, J. (2014). Differentially localized acyl-CoA synthetase 4 isoenzymes mediate the metabolic channeling of fatty acids towards phosphatidylinositol. *Biochim. Biophys. Acta* 1841, 227–239. <https://doi.org/10.1016/j.bbailip.2013.10.018>.
- Magtanong, L., Ko, P.J., To, M., Cao, J.Y., Forcina, G.C., Tarangelo, A., Ward, C.C., Cho, K., Patti, G.J., Nomura, D.K., et al. (2019). Exogenous monounsaturated fatty acids promote a ferroptosis-resistant cell state. *Cell Chem. Biol.* 26, 420–432.e9. <https://doi.org/10.1016/j.chembiol.2018.11.016>.
- Orlando, U.D., Castillo, A.F., Dattilo, M.A., Solano, A.R., Maloberti, P.M., and Podesta, E.J. (2015). Acyl-CoA synthetase-4, a new regulator of mTOR and a potential therapeutic target for enhanced estrogen receptor function in receptor-positive and -negative breast cancer. *Oncotarget* 6, 42632–42650. <https://doi.org/10.18632/oncotarget.5822>.
- Pang, X.Y., Wang, S., Jurczak, M.J., Shulman, G.I., and Moise, A.R. (2017). Retinol saturase modulates lipid metabolism and the production of reactive oxygen species. *Arch. Biochem. Biophys.* 633, 93–102. <https://doi.org/10.1016/j.abb.2017.09.009>.
- Pap, E.H., Drummen, G.P., Winter, V.J., Kooij, T.W., Rijken, P., Wirtz, K.W., Op den Kamp, J.A., Hage, W.J., and Post, J.A. (1999). Ratio-fluorescence microscopy of lipid oxidation in living cells using C11-BODIPY(581/591). *FEBS Lett.* 453, 278–282. [https://doi.org/10.1016/s0014-5793\(99\)00696-1](https://doi.org/10.1016/s0014-5793(99)00696-1).
- Perez, M.A., Magtanong, L., Dixon, S.J., and Watts, J.L. (2020). Dietary lipids induce ferroptosis in *Caenorhabditis elegans* and human cancer cells. *Dev. Cell.* 54, 447–454. <https://doi.org/10.1016/j.devcel.2020.06.019>.
- Piano, V., Benjamin, D.I., Valente, S., Nenci, S., Marrocco, B., Mai, A., Aliverti, A., Nomura, D.K., and Mattevi, A. (2015). Discovery of inhibitors for the ether lipid-generating enzyme AGPS as anti-cancer agents. *ACS Chem. Biol.* 10, 2589–2597. <https://doi.org/10.1021/acschembio.5b00466>.
- Schneider, C.A., Rasband, W.S., and Eliceiri, K.W. (2012). NIH Image to ImageJ: 25 years of image analysis. *Nat. Methods* 9, 671–675. <https://doi.org/10.1038/nmeth.2089>.
- Shannon, P., Markiel, A., Ozier, O., Baliga, N.S., Wang, J.T., Ramage, D., Amin, N., Schwikowski, B., and Ideker, T. (2003). Cytoscape: a software environment for integrated models of biomolecular interaction networks. *Genome Res.* 13, 2498–2504. <https://doi.org/10.1101/gr.1239303>.
- Shimada, K., Skouta, R., Kaplan, A., Yang, W.S., Hayano, M., Dixon, S.J., Brown, L.M., Valenzuela, C.A., Wolpaw, A.J., and Stockwell, B.R. (2016). Global survey of cell death mechanisms reveals metabolic regulation of ferroptosis. *Nat. Chem. Biol.* 12, 497–503. <https://doi.org/10.1038/nchembio.2079>.
- Shui, S., Zhao, Z., Wang, H., Conrad, M., and Liu, G. (2021). Non-enzymatic lipid peroxidation initiated by photodynamic therapy drives a distinct ferroptosis-like cell death pathway. *Redox Biol.* 45, 102056. <https://doi.org/10.1016/j.redox.2021.102056>.
- Soula, M., Weber, R.A., Zilka, O., Alwaseem, H., La, K., Yen, F., Molina, H., Garcia-Bermudez, J., Pratt, D.A., and Birsoy, K. (2020). Metabolic determinants of cancer cell sensitivity to canonical ferroptosis inducers. *Nat. Chem. Biol.* 16, 1351–1360. <https://doi.org/10.1038/s41589-020-0613-y>.
- Sun, X., Ou, Z., Chen, R., Niu, X., Chen, D., Kang, R., and Tang, D. (2016). Activation of the p62-Keap1-NRF2 pathway protects against ferroptosis in hepatocellular carcinoma cells. *Hepatology* 63, 173–184. <https://doi.org/10.1002/hep.28251>.
- Tarangelo, A., Magtanong, L., Biegging-Rolett, K.T., Li, Y., Ye, J., Attardi, L.D., and Dixon, S.J. (2018). p53 suppresses metabolic stress-induced ferroptosis in cancer cells. *Cell Rep.* 22, 569–575. <https://doi.org/10.1016/j.celrep.2017.12.077>.
- Torii, S., Shintoku, R., Kubota, C., Yaegashi, M., Torii, R., Sasaki, M., Suzuki, T., Mori, M., Yoshimoto, Y., Takeuchi, T., and Yamada, K. (2016). An essential role for functional lysosomes in ferroptosis of cancer cells. *Biochem. J.* 473, 769–777. <https://doi.org/10.1042/bj20150658>.
- Wiernicki, B., Dubois, H., Tyurina, Y.Y., Hassannia, B., Bayir, H., Kagan, V.E., Vandenameele, P., Wullaert, A., and Vanden Berghe, T. (2020). Excessive phospholipid peroxidation distinguishes ferroptosis from other cell death modes including pyroptosis. *Cell Death Dis.* 11, 922. <https://doi.org/10.1038/s41419-020-03118-0>.
- Yan, B., Ai, Y., Sun, Q., Ma, Y., Cao, Y., Wang, J., Zhang, Z., and Wang, X. (2021). Membrane damage during ferroptosis is caused by oxidation of phospholipids catalyzed by the oxidoreductases POR and CYB5R1. *Mol. Cell* 81, 355–369.e10. <https://doi.org/10.1016/j.molcel.2020.11.024>.
- Zhu, X.G., Nicholson Puthenveedu, S., Shen, Y., La, K., Ozlu, C., Wang, T., Klompstra, D., Gultekin, Y., Chi, J., Fidelin, J., et al. (2019). CHP1 regulates compartmentalized glycerolipid synthesis by activating GPAT4. *Mol. Cell* 74, 45–58.e7. <https://doi.org/10.1016/j.molcel.2019.01.037>.
- Zille, M., Osés-Prieto, J.A., Savage, S.R., Karuppagounder, S.S., Chen, Y., Kumar, A., Morris, J.H., Scheidt, K.A., Burlingame, A.L., and Ratan, R.R. (2022). Hemin-induced death models hemorrhagic stroke and is a variant of classical neuronal ferroptosis. *J. Neurosci.* 42, 2065–2079. <https://doi.org/10.1523/jneurosci.0923-20.2021>.
- Zou, Y., Henry, W.S., Ricq, E.L., Graham, E.T., Phadnis, V.V., Maretich, P., Paradkar, S., Boehnke, N., Deik, A.A., Reinhardt, F., et al. (2020a). Plasticity of ether lipids promotes ferroptosis susceptibility and evasion. *Nature* 585, 603–608. <https://doi.org/10.1038/s41586-020-2732-8>.
- Zou, Y., Li, H., Graham, E.T., Deik, A.A., Eaton, J.K., Wang, W., Sandoval-Gomez, G., Clish, C.B., Doench, J.G., and Schreiber, S.L. (2020b). Cytochrome P450 oxidoreductase contributes to phospholipid peroxidation in ferroptosis. *Nat. Chem. Biol.* 16, 302–309. <https://doi.org/10.1038/s41589-020-0472-6>.

STAR★METHODS

KEY RESOURCES TABLE

REAGENT or RESOURCE	SOURCE	IDENTIFIER
Antibodies		
4E-BP1	Cell Signaling Technology	Cat# 9644; RRID: AB_2097841
GAPDH	Cell Signaling Technology	Cat# 2118; RRID: AB_561053
Phospho-4E-BP1 (Thr37/46)	Cell Signaling Technology	Cat# 9459; RRID: AB_330985
Phospho-RPS6 (Ser235/236)	Cell Signaling Technology	Cat# 4858; RRID: AB_916156
RPS6	Cell Signaling Technology	Cat# 2217; RRID: AB_331355
Alpha-tubulin, clone DM1A	Fisher Scientific	Cat# MS581P1
680LT Donkey-anti-mouse	LI-COR	Cat# 926-68022; RRID: AB_10715072
680LT Donkey-anti-rabbit	LI-COR	Cat# 926-68023; RRID: AB_10706167
800CW Donkey-anti-mouse	LI-COR	Cat# 926-32212; RRID: AB_621847
800CW Donkey-anti-rabbit	LI-COR	Cat# 926-32213; RRID: AB_621848
ACSL4	Proteintech	Cat# 22401-1-AP; RRID: AB_2832995
AGPS	Proteintech	Cat# 21011-1-AP; RRID: AB_2878789
Chemicals, peptides, and recombinant proteins		
FINO ₂	Abrams et al. (2016)	N/A
Erastin2 (Compound 35MEW28 in Dixon et al., 2014)	Dixon et al. (2014)	N/A
ZINC-69435460	Enamine	Cat# Z1030248250
Bortezomib	Fisher Scientific	Cat# NC0587961; CAS: 179324-69-7
Camptothecin	Fisher Scientific	Cat# AC276721000; CAS: 7689-03-4
C11 BODIPY 581/591 (4,4-difluoro-5-(4-phenyl-1,3-butadienyl)-4-bora-3a,4a-diaza-s-indacene-3-undecanoic acid)	Molecular Probes	Cat# D3861
Hoechst	Molecular Probes	Cat# H1399
SYTOX Green	Molecular Probes	Cat# S7020
RSL3	Selleck Chemical	Cat# S8155; CAS: 1219810-16-8
Vinblastine	Selleck Chemical	Cat# S1248; CAS: 143-67-9
CIL56	Shimada et al. (2016)	N/A
FIN56	Shimada et al. (2016)	N/A
Chloroform	Sigma-Aldrich	Cat# 366927; CAS: 67-66-3
Dimethyl Sulfoxide (DMSO)	Sigma-Aldrich	Cat# 276855; CAS: 67-68-5
Ferrostatin-1	Sigma-Aldrich	Cat# SML0583; CAS: 347174-05-4
Methanol	Sigma-Aldrich	Cat# 34860; CAS: 67-56-1
ML210	Sigma-Aldrich	Cat# SML0521; CAS: 1360705-96-9
Rosiglitazone	Sigma-Aldrich	Cat# R2408; CAS:122320-73-4
Staurosporine	Sigma-Aldrich	Cat# S6942; CAS: 62996-74-1
Thapsigargin	Sigma-Aldrich	Cat# T9033; CAS: 67526-95-8
Deposited data		
Unprocessed western blot images and unprocessed lipidomics data	Dixon (2022), "Context-Dependent Regulation of Ferroptosis Sensitivity", Mendeley Data	https://doi.org/10.17632/fy6c7j78hp.1
Experimental models: Cell lines		
Human: HT-1080	ATCC	Cat# CCL-121; RRID: CVCL_0317
Human: HAP1	Horizon Discovery	Cat# C631; RRID: CVCL_Y019
Human: A549 ^N	Forcina et al. (2017)	N/A

(Continued on next page)

Continued

REAGENT or RESOURCE	SOURCE	IDENTIFIER
Human: HT-1080 ^N	Forcina et al. (2017)	N/A
Human: T98G ^N	Forcina et al. (2017)	N/A
Human: HT-1080 <i>ACSL4</i> ^{KO1}	Magtanong et al. (2019)	N/A
Human: H1299 ^N	Tarangelo et al. (2018)	N/A
Human: A549 ^N <i>ACSL4</i> ^{KO1}	This study	N/A
Human: A549 ^N <i>ACSL4</i> ^{KO2}	This study	N/A
Human: HEK 293 ^N	This study	N/A
Human: HEK 293 ^N <i>ACSL4</i> ^{KO1}	This study	N/A
Human: HEK 293 ^N <i>ACSL4</i> ^{KO2}	This study	N/A
Human: HT-1080 ^N <i>ACSL4</i> ^{KO1}	This study	N/A
Human: HT-1080 ^N <i>ACSL4</i> ^{KO2}	This study	N/A
Human: HT-1080 ^N <i>AGPS</i> ^{Control}	This study	N/A
Human: HT-1080 ^N <i>AGPS</i> ^{KO1}	This study	N/A
Human: HT-1080 ^N <i>AGPS</i> ^{KO2}	This study	N/A
Oligonucleotides		
<i>ACSL4</i> _sg2_F: CACCGGTAGTGGACTC ACTGCACT	Magtanong et al. (2019)	N/A
<i>ACSL4</i> _sg2_R: AAACAGTGCAGTGAGT CCACTACC	Magtanong et al. (2019)	N/A
<i>ACSL4</i> _sg2_conf_F1: ACCCCCAA CTT	Magtanong et al. (2019)	N/A
<i>ACSL4</i> _sg2_conf_R1: GGGACCAGGG AAATCCTAAG	Magtanong et al. (2019)	N/A
<i>ACSL4</i> _sg2_seq: TAAATGGCTAAAC AACACC	Magtanong et al. (2019)	N/A
<i>AGPS</i> _sg1_F: CACCGTGGGTATCTAC TCGCGCATC	This study	N/A
<i>AGPS</i> _sg1_R: AAACGATGCGCGAGTA GATACCCAC	This study	N/A
<i>AGPS</i> _sg1_conf_F1: TGGCCTTAAAC AAAAGGATGT	This study	N/A
<i>AGPS</i> _sg1_conf_R1: TTTGAGACAGAA TCTCGCTCTG	This study	N/A
<i>AGPS</i> _sg1_seq: CAAAGTCTGGGATT ACAG	This study	N/A
Recombinant DNA		
IncuCyte NuLight Red Lentivirus Reagent (EF-1 α , Puro)	Essen BioScience	Cat# 4625
<i>ACSL4</i> -short-S-tag	This study	N/A
<i>ACSL4</i> -long-S-tag	This study	N/A
Software and algorithms		
Cancer Dependency Map		https://depmap.org/portal/
National Center for Biotechnology Information Gene Database		https://www.ncbi.nlm.nih.gov/gene
PubMed		https://pubmed.ncbi.nlm.nih.gov
GraphPad Prism 9.0.1	GraphPad Software, Inc.	https://www.graphpad.com/
Database for Annotation, Visualization and Integrated Discovery (DAVID)	Huang et al. (2009)	https://david.ncifcrf.gov/home.jsp
Microsoft Excel 16.45	Microsoft Corporation	N/A
ImageJ 1.52q	Schneider et al. (2012)	https://imagej.nih.gov/ij
Cytoscape 3.8.0	Shannon et al., 2003	https://cytoscape.org

RESOURCE AVAILABILITY

Lead contact

Further information and requests for resources and reagents should be directed to and will be fulfilled by the Lead Contact, Scott Dixon (sjdixon@stanford.edu).

Materials availability

Plasmids generated in this study will be shared by the [lead contact](#) upon request.

Data and code availability

- Unprocessed western blot images and unprocessed lipidomics data have been deposited at Mendeley and are publicly available as of the date of publication. The DOI is listed in the [Key resources table](#). Microscopy images reported in this paper will be shared by the [lead contact](#) upon request.
- This paper does not report original code.
- Any additional information required to reanalyze the data reported in this paper is available from the [lead contact](#) upon request.

EXPERIMENTAL MODEL AND SUBJECT DETAILS

Cell lines and culture conditions

Validated cell lines were originally obtained from primary vendors, then immediately expanded and frozen in multiple aliquots. Thawed cell lines were validated based on known morphology, growth rates, and ferroptosis sensitivity profiles. Low passage cells (<30 passages) were used for all experiments. HT-1080 cells (gender: male; Cat# CCL-121) were obtained from ATCC (Manassas, VA). HAP1 cells (gender: male with lost Y chromosome) were obtained from Horizon Discovery (Cambridge, UK). Nuclear mKate2-expressing (denoted by superscript 'N') A549^N (gender: male) and HT-1080^N were described previously ([Forcina et al., 2017](#)). HEK 293^N (gender: female) Control cells were described previously ([Perez et al., 2020](#)). HEK 293 ACSL4^{KO1} and ACSL4^{KO2} and HT-1080 Control, ACSL4^{KO1}, and ACSL4^{KO2}, H1299^N (gender: male), and T98G^N (gender: male) were described previously ([Forcina et al., 2017](#); [Magtanong et al., 2019](#); [Tarangelo et al., 2018](#)). Polyclonal populations of all non-mKate2⁺ cell lines used in this study were transduced with lentivirus directing the expression of nuclear-localized mKate2 (Cat# 4476, Essen BioSciences, Ann Arbor, MI, USA) as described previously ([Forcina et al., 2017](#)). A549^N, H1299^N, HEK 293^N, and T98G^N cells were grown in Dulbecco's modified Eagle medium (DMEM, Cat# MT-10-013-CV, Thermo Fisher Scientific, Waltham, MA), 10% fetal bovine serum (FBS, Cat# 26140-079, Gibco), and 0.5 U/mL Pen/Strep (P/S, Cat# 15070-063, Gibco). HT-1080 cells were grown in DMEM supplemented with 10% FBS, 0.5 U/mL P/S and 1x non-essential amino acids (NEAAs, Cat# 11140-050, Gibco). Minus cystine medium was constituted using DMEM (Cat# 17-204-CI, Thermo Fisher Scientific) supplemented with 10% dialyzed FBS (Thermo Fisher Scientific, Cat#26400044), 0.5 U/mL P/S, 1x NEAAs, 201 μ M L-methionine (Cat# M9625, Sigma Aldrich, St. Louis, MO) and 4 mM L-glutamine (Cat# G3126, Sigma Aldrich). HAP1 cells were maintained in low glucose (10 mM), low glutamine (1 mM) DMEM (Cat# 319-162-CL, Wisent), 10% FBS and 0.5 U/mL P/S. Hanks' Balanced Salt solution (HBSS, Cat# 14025-134) and trypsin (Cat# 25200114) were from Gibco. 1x phosphate buffer solution (PBS, Cat# 97062-338) was from VWR (Radnor, PA). For all experiments, cells were trypsinized and counted using a Cellometer Auto T4 cell counter (Nexcelom, Lawrence, MA). Cells were grown and treated in a humidified 37°C, 5% CO₂ incubator, unless specified otherwise.

METHOD DETAILS

Network construction and analysis

All relevant screens reported in PubMed (<https://pubmed.ncbi.nlm.nih.gov>) through the end of December 2020 were analyzed. Loss of function ferroptosis suppressor genetic screens included small interfering RNA (siRNA), short hairpin RNA (shRNA), CRISPR, and gene-trap methods (see [Table S1](#)). All genes defined as functionally significant in each respective screen by the authors' own criteria were initially included in the analysis. Network visualization was performed using Cytoscape 3.8.0 (<https://cytoscape.org>) ([Shannon et al., 2003](#)). For each gene included in [Table S2](#), the gene name reported in the original screen was verified via the National Center for Biotechnology Information Gene database (<https://www.ncbi.nlm.nih.gov/gene>) and, if necessary, updated to the current standard. NCBI gene type was used to annotate pseudogenes, ncRNAs, anti-sense RNAs, and one unknown gene, as well as pinpoint three mouse-only genes that were not included in the final network. In the network, mouse gene names are reported using the human uppercase letter convention for simplicity. The 239 protein coding genes in the network were analyzed using the DAVID bioinformatics resource with standard settings ([Huang et al., 2009](#)). The Functional_Annotations category was used to extract cellular component, molecular function, and biological processes annotations. All significant annotations are reported. A PubMed (<https://pubmed.ncbi.nlm.nih.gov>) search with the term "gene X AND ferroptosis" was performed on March 17, 2022, for each of the 15 genes identified three or more times, to identify the number of abstracts containing each gene in relation to ferroptosis.

Shotgun lipidomics sample treatment, preparation and analysis

The day before the experiment, cells were seeded into 10 cm dishes (Cat# CC7682-3394, USA Scientific, Ocala, FL) as follows: 2 million A549^N Control, *ACSL4*^{KO1}, or *ACSL4*^{KO2} cells/plate for basal level measurements; 1 million HT-1080 Control or *ACSL4*^{KO1} cells/plate x 2 plates for each time point (0, 30, 60, 120 min) of RSL3 treatment; 900,000 HT-1080^N Control, *AGPS*^{KO1}, or *AGPS*^{KO2} cells/plate for basal level measurements. For all experiments, the next day, cells were harvested (for measuring basal levels) or treated for the appropriate time prior to harvesting by trypsinization. Cells were counted and then transferred using a glass Pasteur pipette to conical-bottom glass centrifuge tubes (Cat# 05-569-2, Fisher Scientific) or a 15 mL conical tube. Cells were pelleted (55 x g, 5 min, room temperature) and the supernatant was discarded. Cell pellets in glass centrifuge tubes were immediately frozen at -80°C . Cell pellets in 15 mL conical tubes were resuspended in 0.5 mL 1x PBS, transferred to a flat-bottom, open top glass tube, and immediately frozen at -80°C . Four (A549^N Control and *ACSL4*^{KO1/2} basal levels and HT-1080^N Control and *AGPS*^{KO1/2} basal levels), and three (HT-1080^N Control and *ACSL4*^{KO1} RSL3 time course) independent experiments treated on different days for each condition were collected for analysis. Lipids were then extracted and analyzed exactly as described (Hsieh et al., 2021).

CRISPR/Cas9 genetic screen

A CRISPR/Cas9 screen was performed in HAP1 cells as described (Aregger et al., 2020). Briefly, 100 million HAP1 cells stably expressing Cas9 were transduced with the TKOv3 lentiviral library containing a total of 71,090 guide RNAs, at an M.O.I. of ~ 0.3 and then after 24 h recovery selected in puromycin (1 $\mu\text{g}/\text{mL}$) for 48 h. Cells were then split into three separate populations (Day 0). On day 4, each population was subdivided into erastin2 (1 μM) treatment or DMSO arms, and passaged every three days for a total of three treatment rounds. Cells were harvested on day 15, corresponding to ~ 17 population doublings for control-treated cell populations. Vehicle control and erastin2-treated samples were pelleted, prepared for next generation sequencing, and analyzed as described (Aregger et al., 2020). Quantitative genetic interaction (qGI) scores were computed by comparing the effects on sgRNA representation in the final pools between DMSO control and erastin2-treated conditions.

Cell death analysis using STACK

Cell death was analyzed using the scalable time-lapse analysis of cell death kinetics (STACK) technique. Cell lines stably expressing nuclear-localized mKate2 were incubated in medium with SYTOX Green (SG, 20 nM). Counts of live (mKate2⁺) and dead (SG⁺) objects were obtained from images acquired every 2 or 4 h on the Essen InCuCyte Zoom (Essen BioScience, Ann Arbor, MI). The following image extraction parameter values were used to count all cell lines except as noted below: *for SG⁺ objects*: Adaptive Threshold Adjustment 3; Edge Split On; Edge Sensitivity -7 ; Filter Area min 0 μm^2 max 750 μm^2 ; *for mKate2⁺ objects*: Adaptive Threshold Adjustment 2.5; Edge Split On; Edge Sensitivity -2 ; Filter Area min 50 μm^2 , maximum 8100 μm^2 ; Eccentricity max 0.9; and *for Overlap objects*: Filter area min 50 μm^2 , maximum 8100 μm^2 . For mKate2⁺ objects in A549^N *ACSL4*^{KO1} cells, Adaptive Threshold Adjustment was set to 0.15. For SG⁺ objects in the *ACSL4* rescue experiment, the Filter Area min was set to 40 μm^2 . Counts were exported to Excel (Microsoft Corporation, Redmond, WA) and lethal fraction (LF) scores were computed from mKate2⁺ and SG⁺ counts as described (Forcina et al., 2017), with the additional step of removing 'overlap' double-positive counts from live cell counts at each timepoint (Inde et al., 2020). LF scores were exported to Prism 9.0.1 (GraphPad Software, La Jolla, CA).

Cell death assays

For erastin2 and RSL3 dose response experiments, the day before the experiment, 4,000 HT-1080^N, 5,000 A549^N or 20,000 HEK 293^N Control and *ACSL4*^{KO1/2} cells/well were seeded into a 96-well plate (Cat# 3904, Corning); for HT-1080^N Control and *AGPS*^{KO1/2} cells, 4,000 cells/well were seeded into a 96-well plate (Cat# 3598, Corning). For the remaining lethal compound dose response experiments, the day before the experiment, 5,000 HT-1080^N Control and *ACSL4*^{KO1/2} cells/well were seeded into a 96-well plate. The lethal compounds (and final high concentration) tested were: bortezomib (200 nM), camptothecin (10 μM), CIL56 (20 μM), erastin2 (8 μM), FIN56 (20 μM), FINO₂ (20 μM), RSL3 (8 μM), staurosporine (500 nM), thapsigargin (250 nM) and vinblastine (100 nM). For all compounds, the next day, cells were treated with the appropriate treatment medium containing SYTOX Green (20 nM). Cells were imaged on the Essen InCuCyte Zoom and analyzed using STACK as described above. Three or more independent experiments treated on different days were performed for each condition.

For the cystine deprivation experiments, the day before the experiment, 10,000 HT-1080^N Control and *ACSL4*^{KO1/2} cells/well were seeded into a 96-well plate (Corning). The following day, the medium was removed, and the cells were washed once with HBSS to remove traces of +cystine medium, then treated with standard HT-1080 medium or -cystine medium. Both culture media contained SYTOX Green (20 nM), and then cells were imaged on the Essen InCuCyte Zoom and analyzed using STACK as described above. Three independent experiments treated on different days were performed for each condition.

For pre-treatment experiments, the day before the pre-treatment, cells were seeded as follows: HT-1080^N Control and *ACSL4*^{KO1/2}, H1299^N, or T98G^N: 500 cells/well into a 384-well plate (Corning, Cat# 3764); HT-1080^N Control and *AGPS*^{KO1/2} cells: 2,000 cells/well into a 96-well plate (Corning). For all cell lines, the next day, the cell culture medium was replaced with medium containing the appropriate combination of DMSO (vehicle), rosiglitazone (25 μM), and AGPSi (500 μM). 24 h later, the medium was replaced with the appropriate lethal compound treatment (note that all pre-treatment conditions were maintained during the lethal compound treatments). For all experiments, SYTOX Green (20 nM) was included in the treatment medium. Cells were imaged on the Essen InCuCyte Zoom and analyzed using STACK as described above. Three or more independent experiments treated on different days were performed for each condition.

ACSL4 rescue experiments

The day before the transfection, HT-1080^N ACSL4^{KO1} cells were seeded at 90,000 or 180,000 cells/well into 12-well (for cell death analysis) or 6-well (for western blot analysis) plates (Cat# 3513/6, Corning), respectively. The following day, cells were transfected using Lipofectamine LTX with Plus Reagent (Cat# 15338100, ThermoFisher) according to the manufacturer's protocol. Cells were transfected with plasmids directing the expression of S-tagged ACSL4 short or long isoforms. The short isoform of ACSL4 was PCR amplified from pDONR221-ACSL4 (Harvard Plasmid Database, clone HsCD00042852) and ligated into the NheI and KpnI sites of the pcDNA3.1(-) S-tag plasmid (Christianson et al., 2011). The long isoform of ACSL4 was PCR amplified from the pSin-EF2-ACSL4-HA (a kind gift from Hua Xiao) and ligated into the BamHI and KpnI sites of the pcDNA3.1(-) S-tag plasmid. 1 (cell death) or 2 (western blot analysis) μ g of plasmid DNA (ACSL4^{short}-S-tag or ACSL4^{long}-S-tag) or water (mock) was used for transfection. The transfection mix was left on the cells for 6 h, removed, and replaced with fresh medium. For cell death analysis, the next day the cells were treated \pm RSL3 (1 μ M) \pm ferrostatin-1 (1 μ M). SYTOX Green (20 nM) was included in the lethal treatment mixture. The cells were imaged on the Essen IncuCyte Zoom and analyzed using STACK as described above. Three or more independent experiments treated on different days were performed for each condition. For western blot analysis, the next day the cells were placed on ice, washed once with cold 1x PBS, and then harvested by scraping. The cells were pelleted (500 x g, 5 min, room temperature), and the cell pellets were frozen at -80° C until needed.

CRISPR/Cas9 genome editing and DNA sequencing

Gene-disrupted A549^N cells were generated using ACSL4 single-guide RNA (sgRNA) primers 5'-CACCGGTAGTGGACTCACTGCACT-3' and 5'-AAACAGTGCAGTGAGTCCACTACC-3' that were described previously (Magtanong et al., 2019). Gene-disrupted HT-1080^N cells were generated using sgRNAs designed with CHOP CHOP (<https://chopchop.cbu.uib.no>). The primer sequences used were as follows: AGPS_sg1_F: 5'-CACCGTGGGTATCTACTCGCGCATC-3'; AGPS_sg1_R: 5'-AAACGATGCGCGAGTAGATACCCAC-3'. sgRNA-containing plasmids were cloned using the same protocol described previously (Magtanong et al., 2019). Once monoclonal cell lines were established, genomic DNA from candidate knockout clones was isolated using the NucleoSpin Tissue kit (Cat# 740952, Takara Bio USA Inc, Mountain View, CA). DNA amplicons were generated using the following primers: ACSL4_conf_F1: 5'-ACCCCCAACTCCAACCTCTT-3', ACSL4_conf_R1: 5'-GGGACCAGGGAAATCCTAAG-3' (Magtanong et al., 2019), AGPS_sg1_conf_F1: 5'-TGGCCTTAAAACAAAAGGATGT-3', AGPS_sg1_conf_R1: 5'-TTTGAGACAGAATCTCGCTCTG-3'. Amplicons were purified using a QIAGEN PCR Purification column (Cat# 28106, QIAGEN) and sent for sequencing using the following primers: ACSL4_seq: 5'-TAAAATGGCTAAACAACACC-3' (Magtanong et al., 2019), AGPS_sg1_seq: 5'-CAAAGTGCTGGGATTACAG-3'. Sequence alignments to determine insertions/deletions were performed using TIDE (Brinkman et al., 2014). A549^N ACSL4^{KO1} has a 22 bp deletion and ACSL4^{KO2} has a 13 bp deletion. HT-1080^N AGPS^{KO1} (sg1) has a 4 bp deletion and AGPS^{KO2} (sg1) has a 1 bp deletion. All deletions result in premature stop codons just downstream of the respective cut sites.

Western blot analysis

For INK128-treated cells, four days before treatment, 10,000 HT-1080^N Control or 20,000 HT-1080^N ACSL4^{KO1} cells/well were seeded into 6-well plates (Corning). After four days, cells were treated \pm INK128 (1 μ M). After 24 h, the cells were harvested by trypsinization, pelleted (55 x g, 5 min, room temperature), washed once with 1x PBS, then spun down again (55 x g, 5 min, room temperature). The cell pellets were then immediately stored at -80° C until needed. For A549^N Control, ACSL4^{KO1}, and ACSL4^{KO2} cell lines and for HT-1080^N AGPS Control, AGPS^{KO1}, and AGPS^{KO2} cell lines, at the time of cell collection for gDNA extraction and sequencing, cells (~2–3 million) were also collected for protein extraction and western blot analysis. The cells were collected by trypsinization. The pellet was spun down (55 x g, 5 min, room temperature), washed once with 1x PBS, then spun down again (55 x g, 5 min, room temperature). The cell pellets were then immediately stored at -80° C until needed.

For all cell pellets, on the day of cell lysis, the pellets were thawed on ice and immediately lysed with 75–100 μ L of RIPA/SDS +1:200 Protease Inhibitor Cocktail (Cat# P8340, Sigma-Aldrich) + 5 mM NaF (for \pm INK128 conditions only; Cat# S6776, Sigma-Aldrich). Lysates were sonicated [(1 s on, 1 s off, 60% amplitude) x 10 cycles] and then centrifuged (18,000 x g, 15 min, 4° C). Lysates were quantified using a Pierce BCA assay kit (Cat# 23225, Thermo Scientific) with a standard BSA curve. Equal amounts of protein were combined with 4x Bolt LDS Sample Buffer (Cat# B0007) and 10x Bolt Sample Reducing Agent (Cat# B0009) (Life Technologies), then loaded onto a Bolt 4–12% Bis-Tris Plus Gel (Cat# NW04120BOX; Life Technologies). Protein was transferred to a nitrocellulose membrane using an iBlot2 transfer stack (Cat# IB23001, Life Technologies). The membrane was blocked using Intercept Blocking Buffer (Cat# 927-60001, LI-COR Biotechnology, Lincoln, NE) (1 h, room temperature) and then incubated in the appropriate primary antibody mixture (1.5 h, room temperature or 4° C, overnight). Primary antibodies used were α -ACSL4 (Cat# 22401-1-AP, Proteintech, Rosemont, IL; 1:2,000 dilution), α -AGPS (Cat# 21011-1-AP, Proteintech; 1:1,000 dilution), α -phospho-4E-BP1 (Thr37/46, Cat# 2855T; 1:1,000 dilution, Cell Signaling Technology, Danvers, MA), α -4E-BP1 (Cat# 9644S, Cell Signaling Technology; 1:1,000 dilution), α -GAPDH (Cat# 2118, Cell Signaling Technology; 1:1,000 dilution), α -phospho-RSP6 (Ser235/236, Cat# 4858, Cell Signaling Technology; 1:1,000 dilution), α -RPS6 (Cat# 2217, Cell Signaling Technology; 1:1,000 dilution), and α -alpha-tubulin (Cat# MS581P1, Millipore Sigma, Billerica, MA; 1:4,000 dilution). The primary antibody buffer was Intercept (LI-COR). The membrane was then washed in 1x TBST (5 min, room temperature, three times) and incubated in secondary antibody mixture (1 h, room temperature). Secondary antibodies (LI-COR; 1:15,000 dilution) used were 680LT donkey α -mouse (Cat# 926-68022), 680LT donkey α -rabbit (Cat# 926-68023), 800CW donkey-anti-mouse (Cat# 926-32212), and 800CW donkey α -rabbit (Cat# 925-32213). The secondary antibody buffer was Intercept (LI-COR) or 1:1 TBST:Intercept. The membrane was washed 1x TBST (5 min, room

temperature, three times) and then scanned on an Odyssey CLx Imaging System (LI-COR). When necessary, membranes were stripped with 1x Nitro Stripping Buffer (Cat# 928-40030, LI-COR; 15 min, room temperature), washed three times with 1x PBS (75–100 mL), then blocked in Intercept (LI-COR; 1 h, room temperature) prior to incubation with primary antibody. Two or more independent experiments were performed on different days for each condition.

C11 BODIPY 581/591 imaging

The day before the experiment, 150,000–175,000 HT-1080 Control or *ACSL4*^{KO1} cells/well were seeded into 6-well plates (Corning) with one 22 mm² no. 1.5 glass coverslip in each well. The next day, the cells were treated as described in HT-1080 growth medium for the indicated times. After the treatment, the medium was removed, and the cells were labeled with C11 BODIPY 581/591 (5 μM) and Hoechst (1 μg/mL) dissolved in HBSS. After a 10 min incubation (37°C, 5% CO₂), the C11 BODIPY 581/591 + Hoechst mixture was removed, and fresh HBSS was applied to the cells. The cover slips were removed and mounted in 25 μL HBSS onto glass microscope slides. Cells were imaged using a Zeiss Axio Observer microscope with a confocal spinning-disk head (Yokogawa, Tokyo, Japan), PlanApoChromat 63x/1.4 NA oil immersion objective, and a Cascade II:512 electron-multiplying (EM) CCD camera (Photometrics, Tucson, AZ). Images were processed in ImageJ 1.52q (Schneider et al., 2012). Imaging was performed on two or more independent experiments treated on different days for each condition.

QUANTIFICATION AND STATISTICAL ANALYSIS

Lethal fraction scoring was performed using Microsoft Excel 16.45 (Microsoft). Confocal images were processed in ImageJ 1.52q (U.S. National Institutes of Health, Bethesda, MD). Graphing and statistical analyses were performed using Prism 9.0.1 (GraphPad). Statistical test details are found in the main text and figure legends.

ADDITIONAL RESOURCES

Chemicals and reagents

Erastin2 was synthesized by Acme Bioscience (Palo Alto, CA). RSL3 (Cat# S8155) and INK128 (Cat# S2811) were from Selleck Chemicals (Houston, TX). SYTOX Green (Cat# S7020) was from Life Technologies. Dimethyl sulfoxide (DMSO; Cat# 276,855), ferrostatin-1 (Cat# SML0583), ML210 (Cat# SML0521), methanol (Cat# 34,860), rosiglitazone (Cat# R2408), staurosporine (Cat# S6942), thapsigargin (Cat# T9033), and vinblastine (Cat# V1377) were from Sigma-Aldrich (St. Louis, MO). Bortezomib (Cat# NC0587961) and camptothecin (Cat# AC276721000) were from Fisher Scientific. ZINC-69435460 (AGPSi; Cat# Z1030248250) was from Enamine US Inc. (Cincinnati, OH). C11 BODIPY 581/591 (Cat# D3861) and Hoechst (Cat# H1399) were from Molecular Probes (Eugene, OR). FINO₂ was a gift from Keith Woerpel (New York University, NY, NY). CIL56 and FIN56 were gifts from Rachid Skouta (UMass Amherst, Amherst, MA). C11 BODIPY 581/591 was dissolved in anhydrous methanol, and all other chemicals were dissolved in DMSO. All chemicals were stored at –20°C until use.